Spectral distortion in diffuse molecular luminescence tomography in turbid media

Scott C. Davis,[1,a)] Brian W. Pogue,[1,b)] Stephen B. Tuttle,[1] Hamid Dehghani,[1,2] and Keith D. Paulsen[1]
[1]*Thayer School of Engineering, Dartmouth College, Hanover, New Hampshire 03755, USA*
[2]*School of Computer Science, The University of Birmingham, Edgbaston, Birmingham, B15 2TT, United Kingdom*

(Received 31 March 2008; accepted 7 August 2008; published online 19 May 2009)

The influence of tissue optical properties on the shape of near-infrared (NIR) fluorescence emission spectra propagating through multiple centimeters of tissue-like media was investigated. Fluorescence emission spectra measured from 6 cm homogeneous tissue-simulating phantoms show dramatic spectral distortion which results in emission peak shifts of up to 60 nm in wavelength. Measured spectral shapes are highly dependent on the photon path length and the scattered photon field in the NIR amplifies the wavelength-dependent absorption of the fluorescence spectra. Simulations of the peak propagation using diffusion modeling describe the experimental observations and confirm the path length dependence of fluorescence emission spectra. Spectral changes are largest for long path length measurements and thus will be most important in human tomography studies in the NIR. Spectrally resolved detection strategies are required to detect and interpret these effects which may otherwise produce erroneous intensity measurements. This observed phenomenon is analogous to beam hardening in x-ray tomography, which can lead to image artifacts without appropriate compensation. The peak shift toward longer wavelengths, and therefore lower energy photons, observed for NIR luminescent signals propagating through tissue may readily be described as a beam softening phenomenon. © *2009 American Institute of Physics*. [DOI: 10.1063/1.3116130]

I. INTRODUCTION

Diffuse spectroscopy and optical imaging of tissue using luminescent signals from molecular reporters have become major areas of interest in recent years.[1–4] Broad efforts to develop these strategies for tissue diagnosis and characterization have included exploiting novel biochemical probes, engineering new detection techniques, improving image recovery methods,[5–8] and coupling luminescence detectors to standard imaging systems.[9,10] Extracting meaningful spectroscopic measurements or accurate images of the luminescent activity in tissue requires accurate light transport modeling, which, through substantial growth since the early 1990s,[11] has become fairly mature field of research. While fluorescence molecular imaging and spectroscopy systems for use in small animals[4,10,12–16] have evolved to the point of commercial availability and clinical trials in humans are underway,[17] some of the more subtle complexities of the signal acquisition remain to be examined. One important consideration that has not been investigated in detail, especially in the near-infrared (NIR), is the interaction between the remission spectrum of the reporter and the intervening tissue through which the light transport occurs prior to detection. Specifically, the changes in spectral emission that are intimately linked to the tissue optical properties and the path length of the propagating photons can be measured and quantified. In this study, a systematic evaluation of NIR spectral shift has been completed using simulations and tissue phantoms.

As interest in fluorescence spectroscopy for tissue diagnosis grew, researchers developed methods to compensate for spectral distortion due to tissue optical properties in order to recover intrinsic fluorescence spectra. Original work reported by Wu *et al.*,[18] Durkin *et al.*,[19] and Richards-Kortum *et al.*[20] examined photon migration, Kubelka–Munk and exponential models, respectively, to extract intrinsic autofluorescence signals from the measured distorted spectrum emitted from tissue. In 1996, Durkin and Richards-Kortum[21] compared several modeling approaches and determined that a partial least-squares method yielded an accurate spectral correction. Analytical expressions derived by Gardner *et al.*[22] were used to extract spectra measured through tissue samples on the order of 1 cm. In 2001, Müller *et al.*[23] provided a comprehensive investigation of the effects of absorption and scattering on intrinsic fluorescence extraction based on a photon migration model.

All of these efforts were focused on tissue spectroscopy in the visible spectrum where autofluorescence is high and the significant photon attenuation restricts the distances over which light signals can be measured to a few centimeters. The relatively low attenuation in the NIR allows measurable light penetration over 10 cm, though elastic scattering ensures most photons will change direction within 1 mm of entering the tissue. Photon propagation in the NIR is commonly modeled using the diffusion approximation to the radiative transport equation. While Patterson and Pogue[24] de-

[a)]Electronic mail: scott.c.davis@dartmouth.edu.
[b)]Electronic mail: brian.w.pogue@dartmouth.edu.

veloped a general construct for modeling fluorescence propagation through homogeneous tissues based on diffusion theory, they did not consider the spectral distortion in the detected emissions directly. Some investigators[25,26] have recognized the inherent depth information contained in the spectral distortion and have demonstrated the ability to localize fluorescent layers in tissue simulating phantoms by calculating the ratio of emitted intensity at different wavelengths.

With the development of NIR diffuse tomography for imaging endogenous tissue contrast through centimeters of tissue, extensions of the theoretical framework to incorporate fluorescence detection have been sought to enhance the disease-to-normal tissue contrast and target molecular processes using fluorescent contrast agents.[27–33] Systems have been developed to collect fluorescence intensities from an array of source-detector positions surrounding the tissue of interest and model-based reconstruction techniques have been used to recover fluorescence activity by matching the modeled and measured data using optimization techniques. Most experimental systems employ band-pass or long-pass filters to separate the excitation signal from the fluorescence emission, but rarely has the capability to resolve the fluorescence spectrum been incorporated. Recently, it was shown[10,34] that a spectrally resolved fluorescence tomography scanner that employs spectrometer detection can record fluorescence spectra emitted from tissue. Ignoring the spectral changes in deep tissue imaging may have implications for quantitative accuracy of the recovered images, especially for systems that use relatively large emission wavelength ranges. Since wavelength-dependent attenuation of the fluorescence emission increasingly distorts the measured spectrum as photon path-length increases, the effect is expected to become more pronounced when imaging through larger tissue domains, such as the human breast.

This work investigates NIR fluorescence emission distortion using homogeneous turbid phantoms and diffusion based modeling. The model platform, NIRFAST, has been developed previously[34,35] using the finite element method (FEM), which allows consideration of arbitrarily shaped domains with heterogeneous optical properties. Here, the model system is extended to calculate spectrally resolved emission spectra at discrete wavelengths based on fluorescence spectra of dilute solutions and wavelength-dependent optical properties of tissue. Experimentally measured spectra are compared with spectra generated using the model system. Phantom geometries are representative of the dimensions to be encountered in tomographic imaging of fluorescence activity *in vivo* and the potential implications that spectral distortion has for tomographic imaging of fluorescence are discussed.

II. EXPERIMENTAL DETAILS

A. Phantom design

Phantoms designed to simulate the optical properties of commonly imaged tissue types, typically adipose and fibroglandular breast tissue, were used to investigate the spectral distortion of the detected emission of a distributed fluorescent drug. Two techniques were used to produce tissue-simulating phantoms.[36,37] Liquid phantoms were composed of water or phosphate buffered solution (PBS) and intralipid, which is a fatty suspension that scatters light much like real tissue. Typically, a 1% intralipid solution can be used to mimic tissue scattering in the NIR. The fluorescent contrast agent may then be added in the desired concentration. Absorbing suspensions such as India ink or whole blood may also be added to provide appropriate amounts of optical absorption beyond that introduced by the fluorophore, though these were not used in this study. Though simple to prepare and flexible in terms of composition, the container walls introduce unwanted heterogeneity and light piping effects.

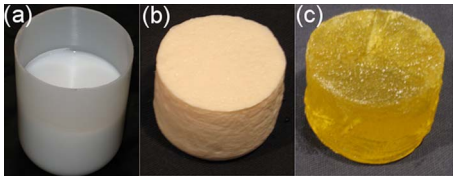

FIG. 1. (Color online) Photographs of phantoms used in this study. A liquid intralipid-based phantom (a) readily allows changing of the fluorophore concentration, while gelatin phantoms containing $TiOB_{2B}$ scatterer shown in (b) eliminate the need for an external container. Gelatin phantoms without scattering material were also used to assess the emission spectra without scatter (c).

Gelatin phantoms composed of gelatin extracted from porcine skin (Sigma Aldrich), TiO_2, blood, and the exogenous contrast agent can be made to closely mimic heterogeneous tissue without artificial boundaries. The mixing procedure used here began by stirring 40 g of type A porcine skin gelatin (Sigma Aldrich) into 500 ml water or PBS. Once dissolved, the solution was heated to about 40 °C in a microwave oven until the solution was fully transparent (approximately 1 min). Immediately after heating, the solution was stirred for 40 min. In cases where scattering was required, 0.4 g of TiO_2 powder (Sigma Aldrich) was slowly added at the beginning of the stirring procedure. It is critical that the media appear homogeneously cloudy with few visible aggregates of TiO_2 after 20 min of stirring. Toward the end of the 40 min, the fluorescent drug was added while the solution was still viscid. Once mixed well, the solution was poured into a mold lined with petroleum jelly and refrigerated for at least 1 h. The cured phantom slid out of the mold easily. Photographs of liquid and gelatin phantoms used in this study are shown in Fig. 1.

The fluorescent drug investigated was Lutetium Texaphyrin (LuTex), a water soluble dye developed as a photodynamic therapeutic sensitizer. It is a texaphyrin based molecule with lutetium in the center to induce a large triplet state splitting.[38] The absorbance and fluorescence emission peaks in dilute solution occur at approximately 735 and 750 nm, respectively. Figure 2 shows a normalized fluorescence emission spectrum of LuTex in a dilute solution of DI (deionized) water measured by a standard fluorometer (Yvon Jobin).

B. Experimental system

The measurement system was a fluorescence tomography scanner designed to detect low levels of light emitted

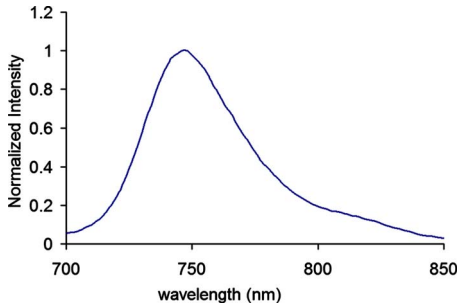

FIG. 2. (Color online) Normalized LuTex fluorescence emission as measured in dilute concentration (2 μg/ml) in DI water.

from thick tissue samples (up to 10 cm). A detailed description of this instrument can be found in Davis *et al.*[10] The imaging array used in the studies reported here consisted of 16 source/detector fibers surrounding a cylindrical tissue phantom as shown in Fig. 3. Each fiber is bifurcated with one branch terminating on a rotary stage, which serially couples light from a 690 nm cw laser diode into any one of the fibers. The other branch couples light from the phantom surface into one of 16 Insight: 400 F Spectroscopy units with cooled charge coupled device (CCD) detection (Princeton Instruments, Acton MA). Automated filter wheels filter the detected light before it enters the spectrograph slit. In the studies presented here, 720 nm long pass filters were used to suppress the excitation light in the measured fluorescence emission signal. In this study, only a single source fiber was illuminated and fluorescence measurements recorded at various locations around the tissue phantom and thus the system was not used to acquire tomographic data.

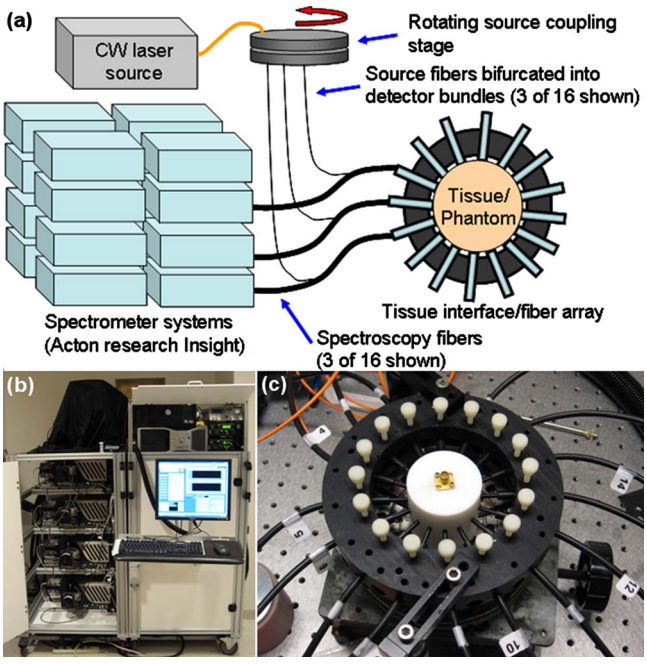

FIG. 3. (Color online) A diagram of the experimental system with 16 spectrometers (Princeton Instruments Inc., Acton MA) is provided in (a) with a photograph shown in (b). Each spectrograph is coupled to a fiber optic, which surrounds a tissue phantom in a circular geometry (c). A homogeneous Teflon calibration phantom is pictured here with the 16 fibers coupled to the exterior in a circle.

C. Modeling light propagation

NIR light propagation in tissue is often modeled by the diffusion approximation, a simplification of the radiative transport equation applicable in media dominated by photon scattering. Modeling fluorescence excitation and emission in tissue is accomplished through a system of diffusion equations, which describe the photon field produced by incident excitation light and fluorescence emission from a distributed fluorophore. Specifically, the excitation source, $q_0(r)$, produces an excitation fluence rate, $\Phi_x(r)$, throughout a medium with optical properties $\mu_{ax}(r)$ and $\mu'_{sx}(r)$ representing the absorption and reduced scattering coefficients, respectively. The field of excitation photons drives the fluorescence emission, which propagates through the tissue subject to optical properties $\mu_{am}(r)$ and $\mu'_{sm}(r)$ at the emission wavelengths. The coupled equations describing this process are presented for the continuous wave case, which matches the capabilities of the instrument,[27,32]

$$-\nabla\kappa_x(r,\lambda_x)\,\nabla\,\Phi_x(r,\lambda_x)+[\mu_{ax}(r,\lambda_x)]\Phi_x(r,\lambda_x)=q_0(r,\lambda_x) \tag{1}$$

$$-\nabla\kappa_m(r,\lambda_m^i)\,\nabla\,\Phi_{fl}(r,\lambda_m^i)+[\mu_{am}(r,\lambda_m^i)]\Phi_{fl}(r,\lambda_m^i)=\Phi_x(r)\,\eta(\lambda_m^i)\mu_{af}(r), \tag{2}$$

where subscripts x and m represent the excitation and emission fluence at wavelengths λ_x and λ_m, respectively, and the diffusion coefficient is $\kappa_{x,m}=1/3(\mu_{ax,m}+\mu'_{sx,m})$. The source term in Eq. (2) is a product of the excitation photon field and the fluorescence yield, defined as $\eta(\lambda_m^i)\mu_{af}(r)$, which itself is a product of the fluorophore's quantum efficiency η and its absorption coefficient, $\mu_{af}(r)$, at the excitation wavelength.

Unlike the excitation field, which is assumed to arise from a light source at a single excitation wavelength, the emission spectrum of the fluorophore can cover several hundred nanometers. To account for this spectral bandwidth in the numerical model, Eq. (2) is discretized over a wavelength range indicated by the index i. Though the excitation field and fluorophore absorption coefficient in the source term of Eq. (2) do not depend on emission wavelength, the fluorescence source strength varies with wavelength based on the shape of the emission spectrum of the fluorophore. This is introduced into the model through a wavelength-dependent fluorescence quantum yield, $\eta(\lambda_m)$. The fluorescence emission propagates through the tissue subject to wavelength-dependent optical properties, $\mu_{am}(r,\lambda_m)$ and $\mu'_{sm}(r,\lambda_m)$, which must be modeled to accurately describe the fluorescence spectrum measured at the tissue surface. In practice, this is accomplished by first calculating the excitation field in Eq. (1), and then solving for the emission field in Eq. (2) at wavelength λ_m^i for each i.

Type III boundary conditions (also known as Robin or mixed) are used to describe the fractional loss of photons at the tissue-air interface. The flux leaving the external boundary is described by

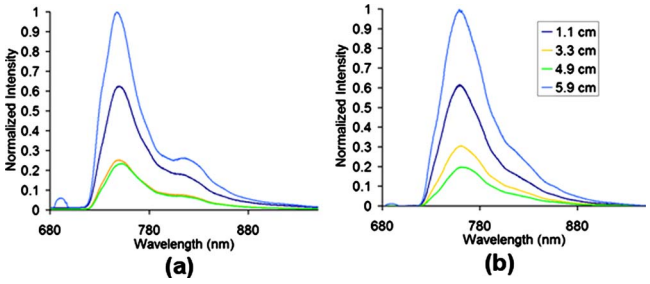

FIG. 4. (Color online) Fluorescence emission of 5 μM LuTex measured in the multispectrometer system in phantoms composed of (a) gelatin and (b) DI water. These spectra represent the nonturbid baselines since neither phantom contained significant scattering media.

$$\Phi_{x,m}(\xi) + 2A\hat{\mathbf{n}} \times \kappa_{x,m}(\xi) \nabla \Phi_{x,m}(\xi) = 0, \tag{3}$$

where ξ is a point on the external boundary and A is derived from Fresnel's law and depends upon the relative refractive index mismatch between tissue, Ω, and air,

$$A = \frac{2/(1 - R_0) - 1 + |\cos\ \theta_c|^3}{1 - |\cos\ \theta_c|^2}, \tag{4}$$

where θ_c is the angle at which propagation from within the domain undergoes total internal reflection at the boundary and

$$R_0 = \frac{(n_1/n_{\mathrm{AIR}} - 1)^2}{(n_1/n_{\mathrm{AIR}} + 1)^2}. \tag{5}$$

The FEM is used to discretize the domain of interest for numerical modeling of the light propagation, which was performed with the NIRFAST software package developed for forward and inverse diffuse tomographic imaging of tissue. A complete description of the numerical implementation can be found elsewhere.[8,34,35,39]

The emission spectrum of LuTex was modeled from 700 to 850 nm in intervals of at most 10 nm. Some intervals were smaller given the availability of information at additional wavelengths. The extinction spectrum of LuTex was measured directly using a Cary 50 UV-visible spectrophotometer (Varian, Inc., Palo Alto CA). Absorption coefficients at each wavelength were calculated as a sum of the constituent chromophores, usually oxygenated and deoxygenated hemoglobin, water, and the exogenous agent of interest, however, since whole blood was not used in the phantom experiments, only water and LuTex were considered in the numerical portion of the study. Published values for the extinction spectrum of water, compiled by Prahl,[40] were used to calculate the absorbing contribution of water. Scattering properties of tissue in the NIR are commonly modeled using an empirical approximation integrated into the NIRFAST software.[41]

III. RESULTS AND DISCUSSION

A. Phantom results

Emission spectra measured through homogeneous gelatin and water phantoms containing 5 μM LuTex and no scattering media are presented in Fig. 4. The phantoms were 60 mm diameter cylindrical shapes with a single source and multiple detectors around the outer surface in one plane.

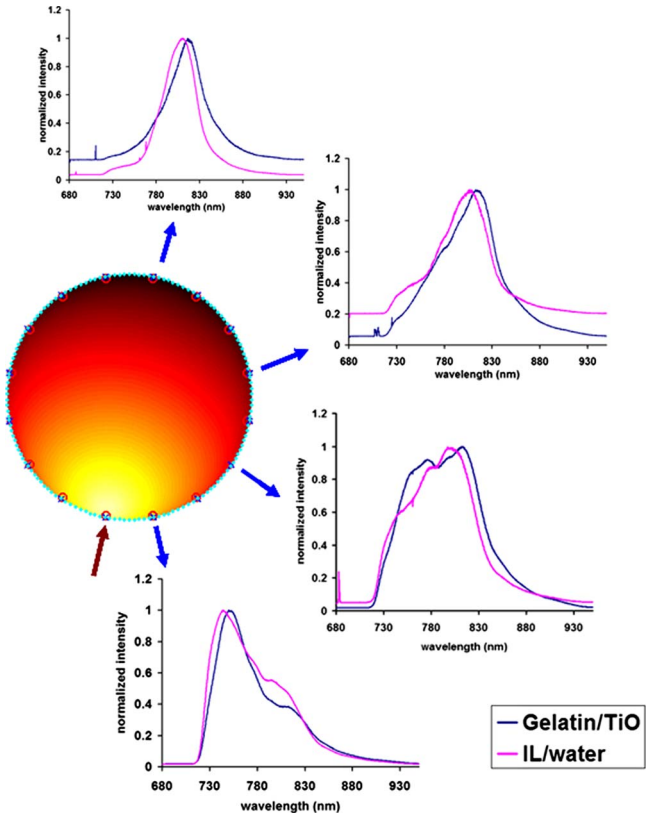

FIG. 5. (Color online) LuTex fluorescence emission experimentally measured at different source-detector distances in homogeneous scattering gelatin and intralipid based phantoms. The circular domain shown represents a cross section of the cylindrical phantom, illustrating the input (red inward-pointing arrow) and output measurement sites (blue outward-pointing arrows). For illustration purposes, the intensity (shown as logarithm of intensity) of the diffuse excitation field is plotted in the circular region.

Data presented are for different source-detector positions on the boundary. As the photon path length increases, the influence of the media changes the emission spectra modestly and thus the emission peak is not significantly distorted when measured through these phantoms.

In turbid phantoms of the same size, the emission spectra change dramatically. LuTex emission spectra measured for a range of source-to-detector distances around a cylindrical turbid phantom are presented in Fig. 5. Data for spectra measured through both gelatin and liquid phantoms are shown and illustrate the significance of the peak distortion through several centimeters of turbid media. Source-detector distances were 1.1, 3.3, 4.9, and 5.9 cm for the spectra included in the figure. Within 1 cm, the measured fluorescence spectrum is similar to the dilute sample, though a secondary peak is evident around 800 nm in both phantoms. As the source-detector distance increases, the spectra are changed more dramatically. The secondary peak becomes increasingly prominent and as the propagation distance increases, the entire spectrum settles to a single peak at 820 nm.

Photon path length may be altered by source-detector geometry or by changes in scattering properties. Figure 6 demonstrates the influence of intralipid concentration on the measured emission spectrum. The spectral changes observed as a result of increasing intralipid concentration are similar to those observed with increasing source-detector distance, as expected.

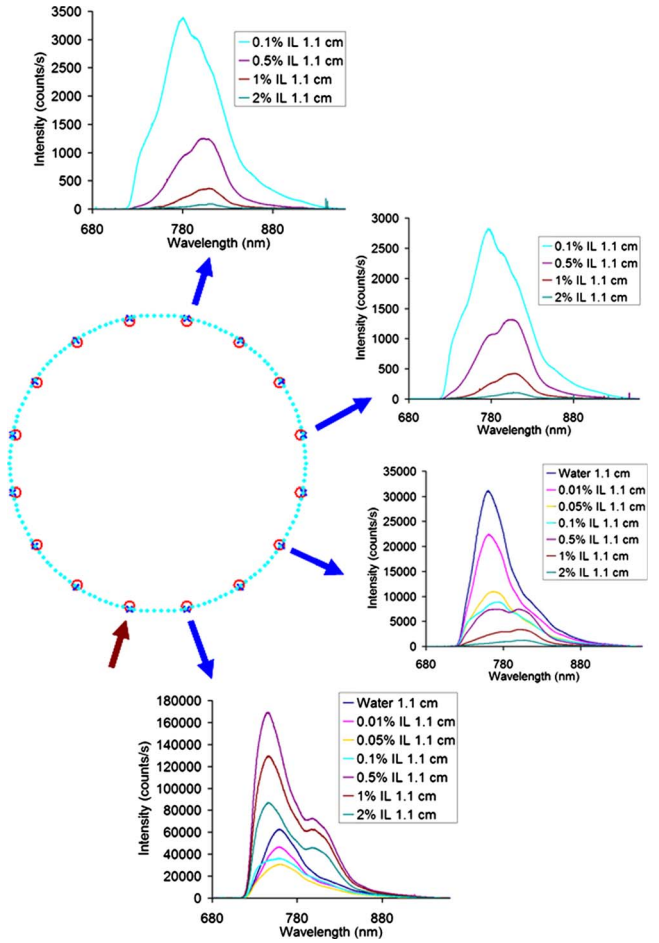

FIG. 6. (Color online) Fluorescence emission spectra through a liquid phantom of DI water and varying concentrations of intralipid are shown. Only spectra measured through intralipid concentrations of 0.1% and above are shown for the two detectors farthest from the source.

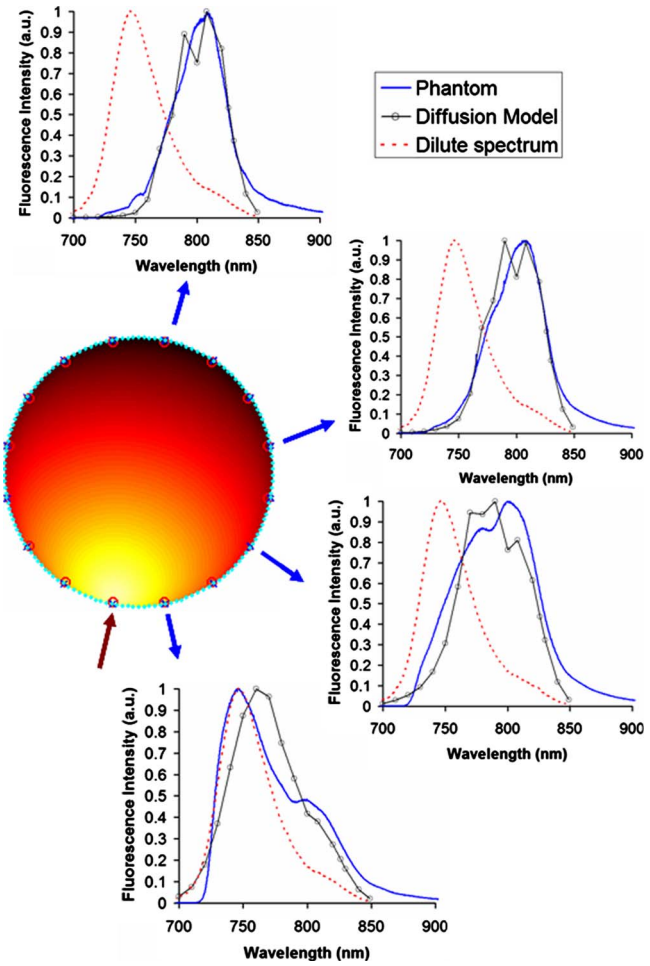

FIG. 8. (Color online) Diffusion based modeling of the fluorescence peak through a 60 mm diameter phantom, similar to Fig. 5. The dilute emission spectrum of LuTex is shown as a dotted line, and the calculated emission spectrum from diffuse emission through the region is shown at discrete wavelengths (black circles). Experimental measurements are shown in blue for intralipid liquid phantoms. The circular domain shown represents a cross section of the cylindrical phantom upon which the intensity (logarithm) of the excitation field calculated from the diffusion equation is plotted for illustration purposes.

B. Diffusion modeling

When modeling photon propagation through the phantoms, it was assumed that the dominant absorbers were water (100%) and LuTex. Extinction spectra of water and LuTex were used to calculate the absorption coefficients at discrete wavelengths across the range covered by the emission spectrum. These values are plotted as a function of wavelength in Fig. 7 and illustrate the large change in absorption due mostly to the fluorophore's absorbance. These values were used to determine the fluorescence intensity at each wavelength throughout the emission spectrum.

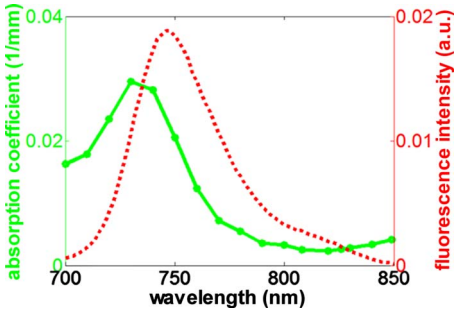

FIG. 7. (Color online) Absorption coefficients of 100% water and 300 nM LuTex are plotted for discrete wavelengths (green line with data points) with LuTex fluorescence emission (red dotted line) in dilute solution, indicating the overlap in absorption and emission at the shorter wavelengths from 700 to 750 nm.

Emission intensities determined from the diffusion model at discrete 10 nm wavelength intervals from 700 to 850 nm are shown in Fig. 8 for the same source-detector positions measured through phantoms and presented in Fig. 5. Experimental data from intralipid phantoms are also plotted for comparison (blue line) and the red dotted line represents the fluorescence peak in a dilute solution. All spectra are normalized to their peaks. Significantly, the general trends recorded in the phantom experiments are also observed for the numerical model. At the detector nearest the source, about 1 cm, the measured fluorescence emission peak is shifted about 10 nm to the red and a small secondary peak is visible at 810 nm, similar to what was observed in the phantom data. This corresponds to a very small bump in the absorption spectrum at 800 nm, which emerges as a dip in the emission spectrum and creates the secondary peak. Increased source-detector distances result in more substantial

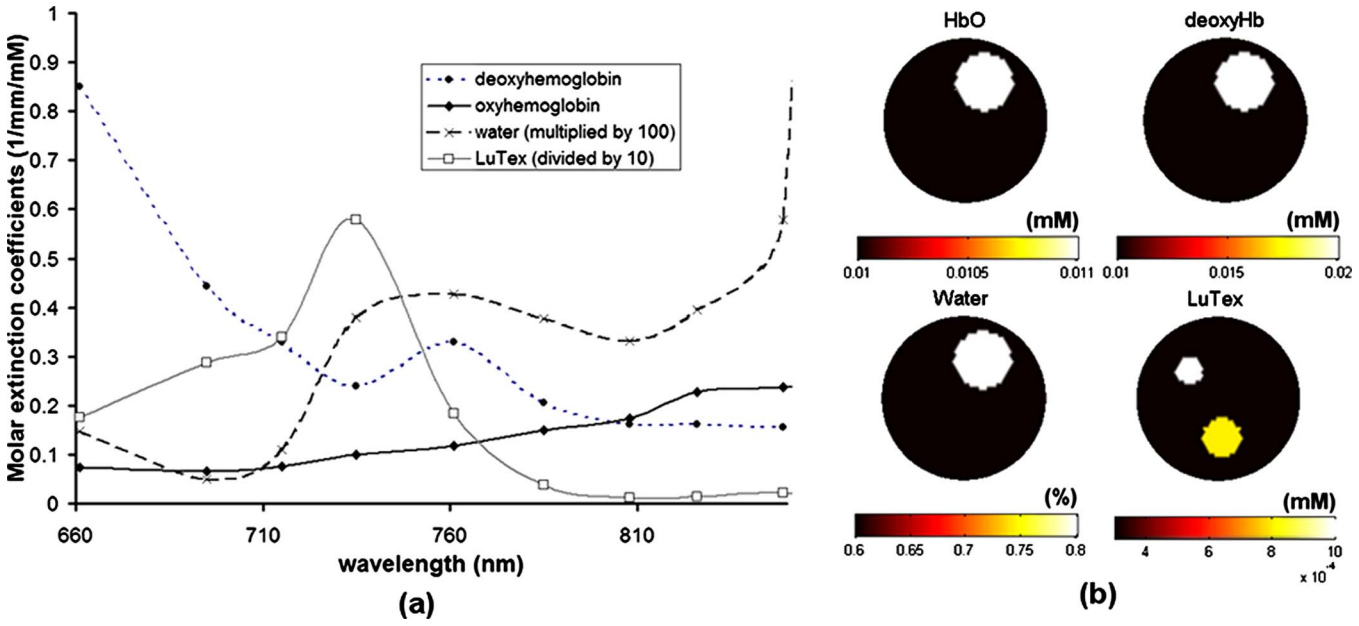

FIG. 9. (Color online) Extinction coefficients of chromophores used in the simulation are shown in (a). These are used to calculate tissue absorption coefficients at any wavelength within the NIR. The simulated domain contains contrasts in the various absorbing constituents, the spatial distributions of which are shown in (b).

changes to the emission spectrum, and an amplification of the influence of the small elevation in absorption at 800 nm. The fluorescence distortion recorded at the detector positioned just over 3 cm from the source results in a peak at 790 nm and a more pronounced dip at 800 nm is observed, producing a stronger secondary peak. The original peak at 750 nm is almost entirely absorbed. At longer source-detector distances, the emission peak settles at 830 nm, similar to the phantom results, although the increase in absorption at 800 nm is more pronounced for the simulation results.

Qualitative assessment of Fig. 8 reveals reasonable agreement between model and experimental observations in turbid phantoms in terms of emission spectrum shape, especially for detector locations far from the source. Pearson correlation coefficients between the model and data were calculated as 0.50, 0.90, 0.97, and 0.94 for the source-detector distances of 1.1, 3.3, 4.9, and 5.9 cm, respectively. The presence of tissue scattering increases the path length of photons propagating through the tissue, which in turn amplifies the influence of the tissue's absorption spectrum. The significance of the peak distortion also indicates that the primary source of fluorescence detected at the far-source detectors is generated close to the excitation source, where the excitation field is most intense, and then propagates through the tissue. This is an expected result since photon penetration depth at the excitation wavelength is lower than within the emission wavelength range due to higher absorption.

C. Implications for fluorescence tomography in deep tissue

The extent of the spectral distortion observed will depend on the fluorophore used, the tissue chromophore composition, and the excitation and measurement geometry. Other drugs used for imaging may experience less distortion than that associated with LuTex. However, the observed phenomenon has implications for quantitative fluorescence tomographic imaging. Clearly, the results presented here indicate that spectrally resolved or band-pass filtering is preferred over long-pass filtering of fluorescence signals.

To demonstrate the extent to which spectrally unresolved data impact fluorescence imaging in deep tissue, a simulated example using an 86 mm circular test domain to represent a coronal slice of a human breast is considered. To create a realistic test domain, tissue optical properties were calculated directly using the extinction spectra of the dominant endogenous chromophores and typical tissue concentrations of those chromophores. LuTex was assumed to be the exogenous fluorophore and extinction coefficients of both endogenous and exogenous chromophores used in this example are shown in Fig. 9 along with the spatial distributions of the chromophores for the coronal slice under consideration. In this case, two small Lutex heterogeneities were included at contrasts of just over 3:1 and 2.5:1 over the background. A large heterogeneity with contrast in hemoglobin and water was also added. Scattering properties were held constant in the domain.

Noise-free data were generated using the forward model described above and signal contamination due to excitation cross talk and tissue autofluorescence was ignored. Images of fluorescence yield were recovered using diffusion-based optimization reconstruction techniques described extensively elsewhere.[34,35] Identical reconstruction algorithms were used to consider data detected using one of two measurement approaches. The first approach assumed that measured data were fully wavelength resolved. The intensity recorded at the tissue surface at a single wavelength was extracted and optical properties at that wavelength were used in the model-based reconstruction algorithm. The second approach simulated an experimental system using only long-pass filters. Since spectral selectivity within the emission spectrum is

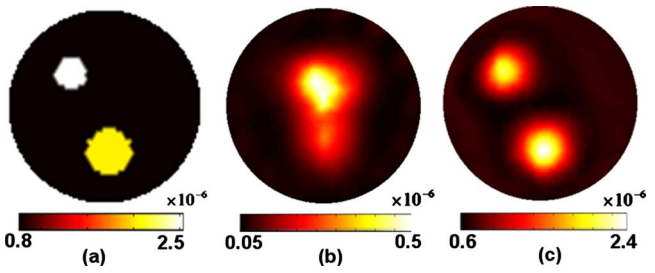

FIG. 10. (Color online) Fluorescence yield of LuTex is calculated from the drug concentration and the fluorescence quantum yield. Based on the concentration of LuTex assumed in Fig. 9, the target fluorescence yield is shown in (a). Reconstructing images from data collected with long-pass filtering can be an intractable problem as shown in (b), while resolving the emitted spectrum allows accurate recovery of the true fluorescence activity, as shown in (c). All images shown are in units of mm^{-1}.

impossible in this configuration, the measured spectrum at each detector was integrated. Tissue optical properties were chosen to match those at 750 nm, the fluorescence emission peak in dilute solution. Although the spatial heterogeneity of these optical properties was assumed to be known exactly at this wavelength, the lack of spectral resolution does not account for the variation in optical properties across the integrated spectrum.

Reconstructed images using both techniques are shown alongside the target image of fluorescence yield in Fig. 10. The only difference between the two approaches arises from the handling of the detected fluorescence spectra. Images reconstructed using spectrally resolved data at a single wavelength show accurate recovery of fluorescence activity in the domain. Recovered values in the contrast enhanced regions are slightly off target values, although this is expected given the reported trade-off between enhanced region size and recovered contrast.[42] Overall, quantification and localization are excellent. Certainly, this is to be expected given the simple geometry and noise-free data. However, the data-model misfit error introduced by integrating the full spectrum is too much for the imaging algorithm and complete breakdown in imaging performance is observed, even for this relatively simple domain. The data provide no ability to localize or quantify fluorescence contrast enhancement. The failure of the algorithm using these data indicates that the long-pass filtering approach is intractable for experimental imaging, making spectrally resolved detection imperative for accurate image recovery. The extent to which this applies can be investigated by varying the wavelength range over which the spectrum is integrated to determine the widest filter band width at which image artifacts are insignificant.

The dramatic influence of chromophore absorption on the fluorescence spectrum leaving the tissue clearly indicates that the spectral shape contains information related to the location of the emitting source. It is reasonable to postulate that this information can be exploited to improve tomographic fluorescence imaging *in vivo*, presuming spatial distributions of tissue chromophore concentrations are known *a priori* and the measured emission spectrum contains insignificant background signal. Similar approaches have been used in bioluminescence imaging of small animals[43,44] and may easily be adapted to fluorescence image reconstruction.

IV. SUMMARY

The problems of spectral shift are well known in many imaging applications such as x-ray computed tomography, where high atomic number materials can cause a larger than expected attenuation of the longer wavelength photons, and shift the spectrum to higher energies, a phenomenon known as beam hardening.[45] Luminescent peaks propagating through tissue in the NIR, on the other hand, exhibit shifting toward lower energy photons, a phenomenon which softens the photon field. The principles in both cases are quite similar in that the spectrum to be detected is not attenuated equally as it traverses the medium.

A dramatic fluorescence emission peak shift in the NIR was demonstrated in tissue simulating phantoms, and this effect is especially pronounced when the tissue path lengths over which the light signal is measured become larger. Thus, the effect will likely have a greater impact on imaging human organs than in small animal applications. The influence of tissue absorption was shown to produce the spectral distortion, an effect amplified by increasing photon path lengths caused by tissue photon scattering or extended source-to-detector distances. Emission spectra escaping the tissue phantom can be modeled reasonable well using a finite element formulation of diffusion theory, especially for source-detector distances over 2 cm. These spectral changes should be considered for fluorescence tomography imaging through several centimeters of tissue. Use of spectrally resolved detection allows quantification of this change, and may be the only reliable way to track intensity changes, which would otherwise appear erroneous.

ACKNOWLEDGMENTS

This work was funded by the National Institutes of Health Grant Nos. RO1 CA109558, RO1 CA69544, and U54 CA105480, Philips Research Hamburg, as well as Department of Defense Breast Cancer pre-doctoral fellowship BC051058.

[1] V. Ntziachristos, J. Ripoll, L. V. Wang, and R. Weissleder, Nat. Biotechnol. **23**, 313 (2005).
[2] V. Ntziachristos, G. Turner, J. Dunham, S. D. Windsor, A. Soubret, J. Ripoll, and H. A. Shih, J. Biomed. Opt. **10**, 064007 (2005).
[3] W. Wang, S. Ke, Q. Wu, C. Charnsangavej, M. Gurfinkel, J. G. Gelovani, J. L. Abbruzzese, E. M. Sevick-Muraca, and C. Li, Molecular Imaging **3**, 343 (2004).
[4] G. Zacharakis, J. Ripoll, R. Weissleder, and V. Ntziachristos, IEEE Trans. Med. Imaging **24**, 878 (2005).
[5] E. E. Graves, J. P. Culver, J. Ripoll, R. Weissleder, and V. Ntziachristos, J. Opt. Soc. Am. A Opt. Image Sci. Vis. **21**, 231 (2004).
[6] S. Srinivasan, B. W. Pogue, C. M. Carpenter, P. K. Yalavarthy, and K. D. Paulsen, Med. Phys. **34**, 4545 (2007).
[7] G. M. Turner, G. Zacharakis, A. Soubret, J. Ripoll, and V. Ntziachristos, Opt. Lett. **30**, 409 (2005).
[8] P. K. Yalavarthy, B. W. Pogue, H. Dehghani, and K. D. Paulsen, Med. Phys. **34**, 2085 (2007).
[9] C. M. Carpenter, B. W. Pogue, H. Jiang, H. Dehghani, K. D. Paulsen, W. A. Wells, J. Forero, C. Kogel, J. B. Weaver, S. P. Poplack, and P. A. Kaufman, Opt. Lett. **32**, 933 (2007).
[10] S. C. Davis, B. W. Pogue, R. Springett, C. Leussler, P. Mazurkewitz, S. B. Tuttle, S. L. Gibbs-Strauss, S. S. Jiang, H. Dehghani, and K. D. Paulsen, Rev. Sci. Instrum. **79**, 064302 (2008).
[11] S. R. Arridge, Inverse Probl. **15**, R41 (1999).
[12] N. Deliolanis, T. Lasser, D. Hyde, A. Soubret, J. Ripoll, and V. Ntziach-

ristos, Opt. Lett. **32**, 382 (2007).
[13]H. Meyer, A. Garofalakis, G. Zacharakis, S. Psycharakis, C. Mamalaki, D. Kioussis, E. N. Economou, V. Ntziachristos, and J. Ripoll, Appl. Opt. **46**, 3617 (2007).
[14]S. V. Patwardhan, S. R. Bloch, S. Achilefu, and J. P. Culver, Opt. Express **13**, 2564 (2005).
[15]J. Ripoll, R. B. Schulz, and V. Ntziachristos, Phys. Rev. Lett. **91**, 103901 (2003).
[16]R. B. Schulz, J. Ripoll, and V. Ntziachristos, Opt. Lett. **28**, 1701 (1701).
[17]A. Corlu, R. Choe, T. Durduran, M. A. Rosen, M. Schweiger, S. R. Arridge, M. D. Schnall, and A. G. Yodh, Opt. Express **15**, 6696 (2007).
[18]J. Wu, M. S. Feld, and R. P. Rava, Appl. Opt. **32**, 3585 (1993).
[19]A. J. Durkin, S. Jaikumar, N. Ramanujam, and R. Richards-Kortum, Appl. Opt. **33**, 414 (1994).
[20]R. Richards-Kortum, R. P. Rava, M. Fitzmaurice, L. L. Tong, N. B. Ratliff, J. R. Kramer, and M. S. Feld, IEEE Trans. Biomed. Eng. **36**, 1222 (1989).
[21]A. J. Durkin and R. Richards-Kortum, Lasers Surg. Med. **19**, 75 (1996).
[22]C. M. Gardner, S. L. Jacques, and A. J. Welch, Appl. Opt. **35**, 1780 (1996).
[23]M. G. Müller, I. Georgakoudi, Q. Zhang, J. Wu, and M. S. Feld, Appl. Opt. **40**, 4633 (2001).
[24]M. S. Patterson and B. W. Pogue, Appl. Opt. **33**, 1963 (1994).
[25]J. Svensson and S. Andersson-Engels, Opt. Express **13**, 4263 (2005).
[26]J. Swartling, J. Svensson, D. Bengtsson, K. Terike, and S. Andersson-Engels, Appl. Opt. **44**, 1934 (2005).
[27]D. Y. Paithankar, A. U. Chen, B. W. Pogue, M. S. Patterson, and E. M. Sevick-Muraca, Appl. Opt. **36**, 2260 (1997).
[28]H. B. Jiang, Appl. Opt. **37**, 5337 (1998).
[29]D. J. Hawrysz and E. M. Sevick-Muraca, Neoplasia **2**, 388 (2000).
[30]M. J. Eppstein, D. J. Hawrysz, A. Godavarty, and E. M. Sevick-Muraca, Proc. Natl. Acad. Sci. U.S.A. **99**, 9619 (2002).
[31]V. Ntziachristos and R. Weissleder, Opt. Lett. **26**, 893 (2001).
[32]A. B. Milstein, O. Seungseok, K. J. Webb, C. A. Bouman, Q. Zhang, D. A. Boas, and R. P. Millane, Appl. Opt. **42**, 3081 (2003).
[33]A. Godavarty, A. B. Thompson, R. Roy, M. Gurfinkel, M. J. Eppstein, C. Zhang, and E. M. Sevick-Muraca, J. Biomed. Opt. **9**, 488 (2004).
[34]S. C. Davis, H. Dehghani, J. Wang, S. Jiang, B. W. Pogue, and K. D. Paulsen, Opt. Express **15**, 4066 (2007).
[35]D. S. Kepshire, S. C. Davis, H. Dehghani, K. D. Paulsen, and B. W. Pogue, Appl. Opt. **46**, 1669 (2007).
[36]S. Jiang, B. W. Pogue, T. O. McBride, M. M. Doyley, S. P. Poplack, and K. D. Paulsen, J. Electron. Imaging **12**, 613 (2003).
[37]B. Pogue and M. Patterson, J. Biomed. Opt. **11**, 0411021 (2006).
[38]G. Kostenich, A. Orenstein, L. Roitman, Z. Malik, and B. Ehrenberg, Photochem. Photobiol. **39**, 36 (1997).
[39]H. Dehghani, B. W. Pogue, S. Jiang, B. Brooksby, and K. D. Paulsen, Appl. Opt. **42**, 3117 (2003).
[40]S. A. Prahl.
[41]S. Srinivasan, B. W. Pogue, S. Jiang, H. Dehghani, and K. D. Paulsen, Appl. Opt. **44**, 1858 (2005).
[42]S. C. Davis, B. W. Pogue, H. Dehghani, and K. D. Paulsen, J. Biomed. Opt. **10**, 1 (2005).
[43]A. J. Chaudhari, F. Darvas, J. R. Bading, R. A. Moats, P. S. Conti, D. J. Smith, S. R. Cherry, and R. M. Leahy, Phys. Med. Biol. **50**, 5421 (2005).
[44]H. Dehghani, S. C. Davis, H. Jiang, B. W. Pogue, K. D. Paulsen, and M. S. Patterson, Opt. Lett. **31**, 365 (2006).
[45]J. T. Bushberg, J. A. Seibert, J. Edwin, M. Leidholdt, and J. M. Boone, *The Essential Physics of Medical Imaging*, 2nd ed. (Lippincott Williams & Wilkins, Philadelphia, 2002).